Supplementary Information

Orientation-engineered Epitaxial $BiVO_4$ Thin Films for Efficient Photoelectrochemical Glycerol Valorization

*Minjoo Lee,[†a] Jun Beom Hwang,[†a] Yoonsung Jung,[a] Jiwoong Yang,[a] ,Yunseo Jang,[a] Inhyeok Oh,[a] Yejoon Kim,[a] Yong-Ryun Jo[b] and Sanghan Lee[*a]*

[a] *Department of Materials Science and Engineering, Gwangju Institute of Science and Technology, Gwangju, 61005, Republic of Korea. E-mail: sanghan@gist.ac.kr*
[b] *GIST Advanced Institute of Instrumental Analysis (GAIA), Electron Microscopy Laboratory, Gwangju Institute of Science and Technology, Gwangju, 61005, Republic of Korea*
Electronic Supplementary Information (ESI) available: See DOI: 10.1039/x0xx00000x

Experimental section

Preparation of epitaxial $BiVO_4$ thin film photoanodes

Epitaxial $BiVO_4$ thin films with distinct crystallographic orientations were prepared using pulsed laser deposition (PLD) equipped with a KrF excimer laser (Coherent COMPexPro 205F, $\lambda = 248$ nm). For the c-axis-oriented $BiVO_4$ (00*l*) films, an indium tin oxide (ITO) buffer layer was first deposited on a YSZ (001) substrate at 600 °C under an oxygen partial pressure of 100 mTorr, followed by $BiVO_4$ deposition at 450 °C and 150 mTorr. In the case of the b-axis-oriented $BiVO_4$ (0*k*0) films, a $SrRuO_3$ (SRO) buffer layer was grown on an STO (001) substrate at 680 °C and 100 mTorr, and the subsequent $BiVO_4$ layer was deposited at 350 °C under 150 mTorr of oxygen. All the layers were sequentially deposited without external processes, and their thicknesses were determined by controlling the number of laser pulses. The selection of substrate and buffer layer combinations was optimized to minimize lattice mismatch and ensure similar electrical conductivities between ITO and SRO bottom electrodes, as described in Fig. 1a.

Characterization of epitaxial $BiVO_4$ thin films

The crystallinity and phase of the films were analyzed using a Rigaku SmartLab X-ray diffractometer equipped with a 9 kW rotating anode X-ray source ($\lambda = 1.5418$ Å). θ-2θ scans, reciprocal space mapping (RSM), and φ-scan analyses were performed to characterize the structural properties of the films. The surface morphology and the thickness of as-prepared photoanodes were analyzed by scanning electron microscope (SEM, JSM-7500F, JEOL). The chemical properties were estimated using X-ray photoelectron spectroscopy (XPS, NEXAS, Thermo Fisher Scientific). Raman spectroscopy was performed using a LabRAM HR Evolution spectrometer (Horiba) equipped with a 532 nm excitation laser. The additional structural characteristics were determined using transmission electron microscopy (TEM, FEI Tecnai G2 F30 S-Twin). The optical properties were measured using ultraviolet–visible (UV–vis) absorption spectroscopy (LAMBDA 950, Perkin Elmer). Atomic force microscopy (AFM, Park Systems NX10) was employed to obtain surface topography images. All characterizations were performed at the GIST Advanced Institute of Instrumental Analysis (GAIA).

Photoelectrochemical measurement

Electrochemical characteristics were investigated using a potentiostat (Ivium-n-Stat, Ivium Technologies) with a 150 W Xe lamp (Model 10500, ABET Technology) equipped with an AM 1.5G optical filter. The light intensity at the sample surface was calibrated to 1-sun (100 $mW \cdot cm^{-2}$) using a photodiode (Bunkokeiki Co., Ltd.). All photoelectrochemical measurements were conducted within a three-electrode system, situated in an H-type quartz cell, wherein the working electrode and counter electrode were partitioned by a Nafion membrane. The electrodes were constructed with the $BiVO_4$ photoanodes, an Ag/AgCl electrode, and a platinum coil for the working, reference, and counter electrodes, respectively. The potentials, relative to the Ag/AgCl electrode, were converted to the reversible hydrogen electrode (RHE) using the Nernst equation; $E_{RHE} = E_{Ag/AgCl} + 0.0591 \times pH + 0.197$, where E_{RHE} is the converted potential, and $E_{Ag/AgCl}$ is the reference potential of the Ag/AgCl electrode. Linear sweep voltammetry (LSV) was performed with a scan rate of 10 $mV \cdot s^{-1}$ and a scan step size of 10 mV. Electrochemical impedance spectroscopy (EIS) was performed at potentials of 1.23 V_{RHE}, in a frequency range of 100 kHz to 0.1 Hz under illumination. The equivalent circuit used to fit the Nyquist plots consisted of a series resistor (R_1), which includes the sheet resistance of the ITO and SRO substrates and two resistor-capacitor circuits, where R_2 and CPE_2 are the charge-transfer resistance and double-layer capacitance across the bulk photoanodes. Intensity modulated photocurrent spectroscopy (IMPS) measurements were carried out using a blue LED (peak wavelength 450 nm) controlled by a frequency-response analyzer. The light intensities were modulated with a depth of 10%, and the frequency was lowered from 10 kHz down to 0.1 Hz.

Efficiency calculation

The water oxidation photocurrent density (J_{water}) of photoelectrodes can be determined as a product of light absorption current (J_{abs}) by the loss factors by the following equation

$$J_{water} = J_{abs} \times \eta_{sep} \times \eta_{trans}$$

Here, η_{sep} is charge separation efficiency and η_{trans} is surface charge transfer efficiency. The J_{water} was calculated with AM 1.5G spectral irradiance (N_{ph}, mW m^{-2} nm^{-1}) and absorption efficiency (η_{abs}) from absorbance (A), using the following equations.

$$J_{abs} = \int_{300}^{\lambda_c} \frac{\lambda}{1240} \times N_{ph}(\lambda) \times \eta_{abs}(\lambda)\, d\lambda$$

$$\eta_{abs} = 1 - 10^{-A(\lambda)}$$

When a hole scavenger (Na_2SO_3) is added to the electrolyte, surface recombination is suppressed and η_{trans} generally reaches 100 %. Thus, η_{sep} and η_{trans} are expressed by the following equations;

$$\eta_{sep} = \frac{J_{sulfite}}{J_{abs}} \times 100\ \%$$

$$\eta_{trans} = \frac{J_{water}}{J_{sulfite}} \times 100\ \%$$

Where $J_{sulfite}$ is sulfite oxidation photocurrent density in a mixed solution of 0.1 M KOH and 1.0 M Na_2SO_3.

Quantification analysis

The quantification of products was performed using high performance liquid chromatography (HPLC) (Alliance 2695, Waters) systems, equipped with an Aminex HPX 87-H column (9.0 μm, 300 mm × 7.8 mm, Bio-Rad) and a UV detector (waters 2487, waters). The column temperature was consistently maintained at 65 °C, and the UV detector wavelength was set at 210 nm for the detection of oxidation products. A 20 μL sample of the electrolyte, where the oxidation occurred, was injected into the HPLC system using isocratic elution with 5 mM sulfuric acid at a flow rate of 0.6 mL min^{-1}. Nuclear magnetic resonance (NMR, JNM-ECX400, Jeol) was utilized to supplement the qualitative analysis using deuterium oxide. The faradaic efficiency (η) of the liquid products was calculated using the following equation;

$$Faradaic\ efficiency = \frac{z \times mol \times \frac{V}{u}}{Q}$$

, where mol is the number of moles of liquid products, V is the total volume of the electrolyte, u is the injection volume of HPLC, and Q is the total charge passed through the electrode.

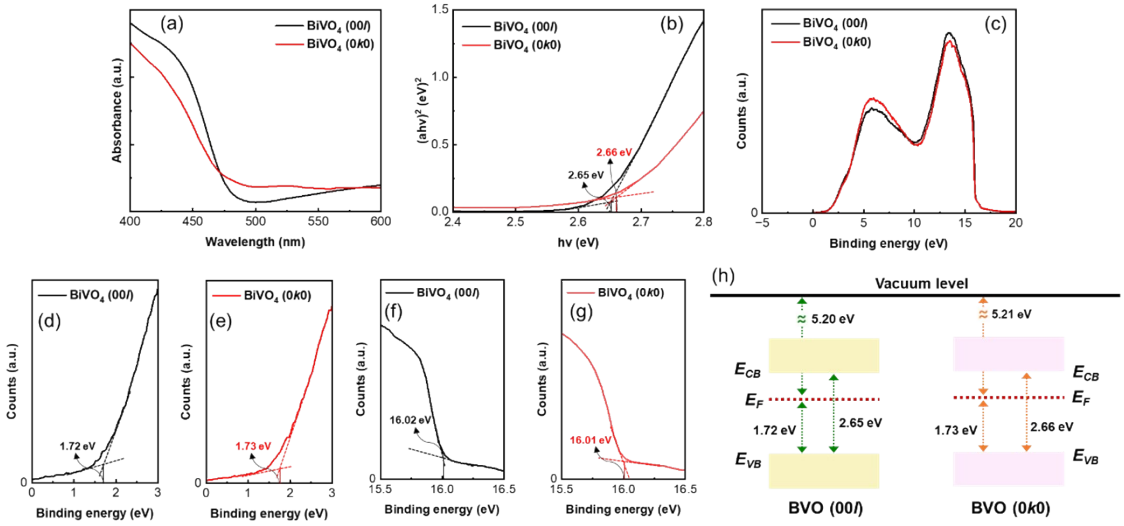

Fig. S1 (a) Ultraviolet–visible (UV–vis) absorbance spectra of $BiVO_4$ (00*l*) and (0*k*0) films. (b) Tauc plots used to estimate the optical bandgap. (c) Ultraviolet photoelectron spectroscopy (UPS) survey spectra of $BiVO_4$ (00*l*) and (0*k*0) films. (d,e) UPS valence band spectra near the Fermi level for $BiVO_4$ (00*l*) and (0*k*0), respectively, showing the valence band onset. (f,g) Secondary electron cutoff regions used to determine the work function for $BiVO_4$ (00*l*) and (0*k*0), respectively. (h) Schematic band diagrams constructed from the measured work functions and valence band onsets from UPS together with the optical bandgaps obtained from the Tauc analysis. Work function values were determined from the UPS secondary electron cutoff using $\Phi = h\nu - E_{cutoff}$, where $h\nu = 21.22$ eV for He I radiation. The cutoff energy (E_{cutoff}) was obtained by linearly extrapolating the leading edge of the secondary electron cutoff to the baseline. The valence band onset relative to the Fermi level was extracted from the UPS valence band spectra by linear extrapolation of the leading edge near the valence band maximum. The optical bandgap (E_g) was estimated from Tauc plots using the UV–vis absorption spectra. The band diagrams were constructed on the vacuum level scale by combining Φ and the valence band onset to determine the VBM position relative to E_{vac}, and by placing the CBM at ECB = EVB + Eg.

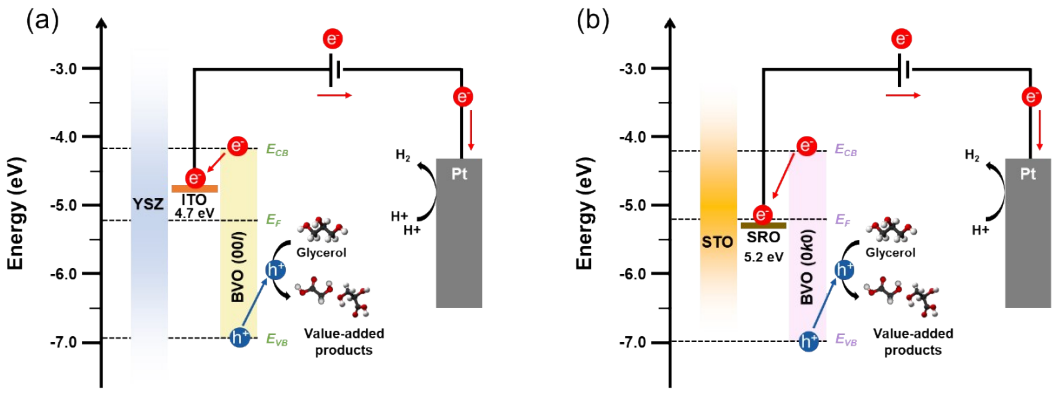

Fig. S2 Schematic band diagrams illustrating the energy level alignment and charge transfer pathways in the two epitaxial $BiVO_4$ photoanode heterostructures coupled with a Pt cathode for H_2 evolution. (a) $BiVO_4$ (00*l*)/ITO/YSZ and (b) $BiVO_4$ (0*k*0)/SRO/STO. The $BiVO_4$ band edge positions were determined from UV–vis absorption and UPS (Fig. S1), while the work functions of ITO and SRO were taken from reported values.[1, 2]

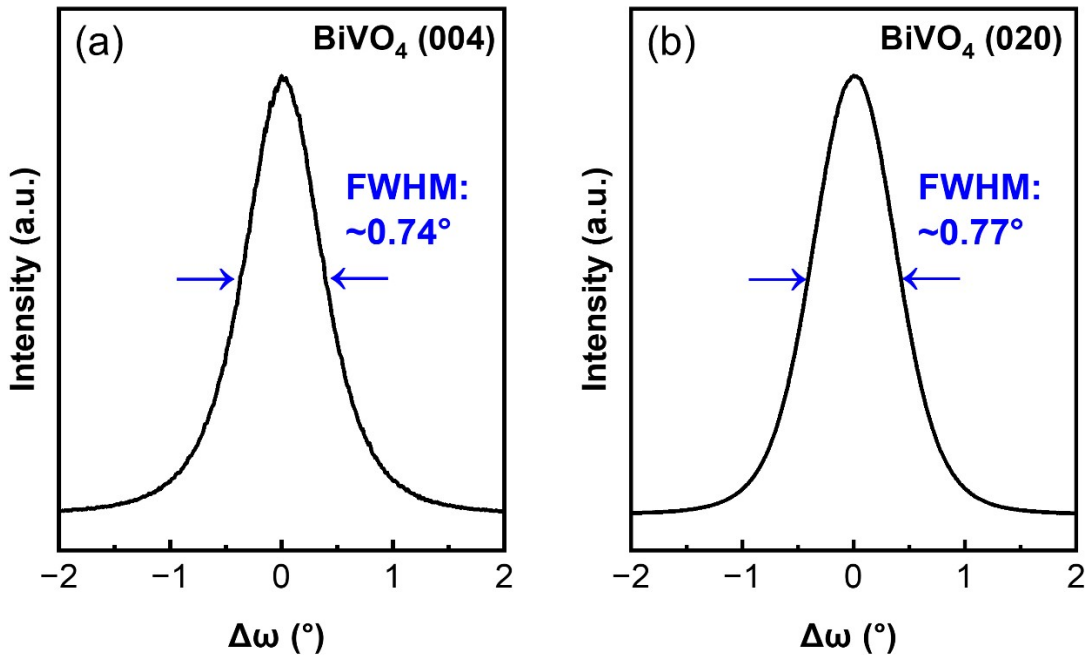

Fig. S3 XRD reflection rocking curves and full width at half maximum (FWHM) values of (a) $BiVO_4$ (004) diffraction peak for an epitaxial $BiVO_4$ (00*l*) thin film and (b) $BiVO_4$ (020) diffraction peak for epitaxial $BiVO_4$ (0*k*0) thin film.

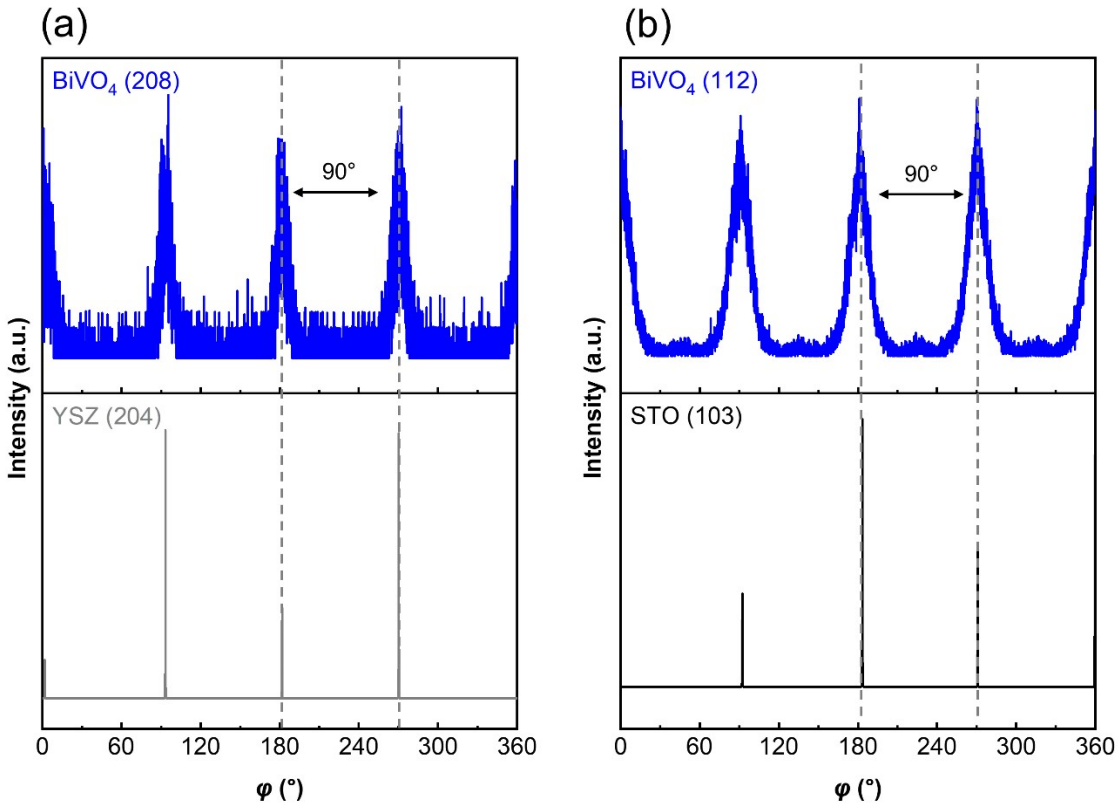

Fig. S4 ϕ scans of (a) $BiVO_4$ (00*l*) and (b) $BiVO_4$ (0*k*0) samples showing the in-plane symmetries and orientation relationships.

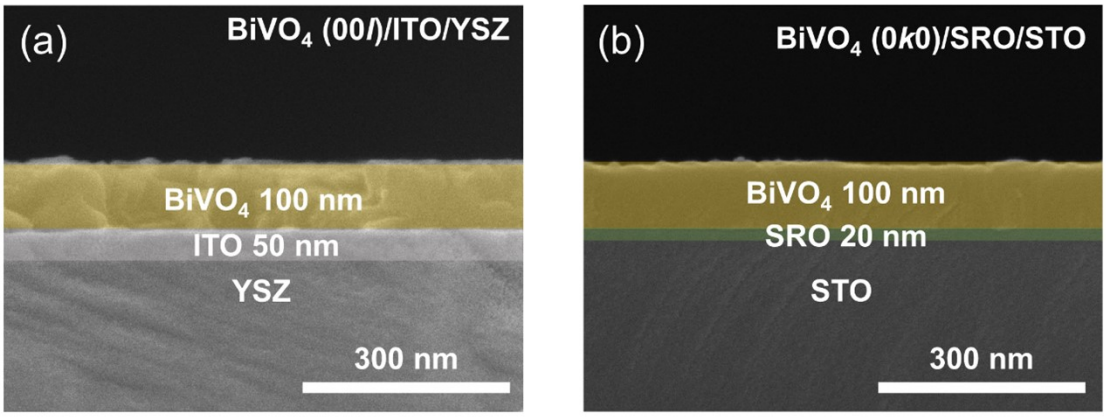

Fig. S5 SEM cross-sectional images of (a) $BiVO_4$ (00*l*) and (b) $BiVO_4$ (0*k*0) thin films, respectively.

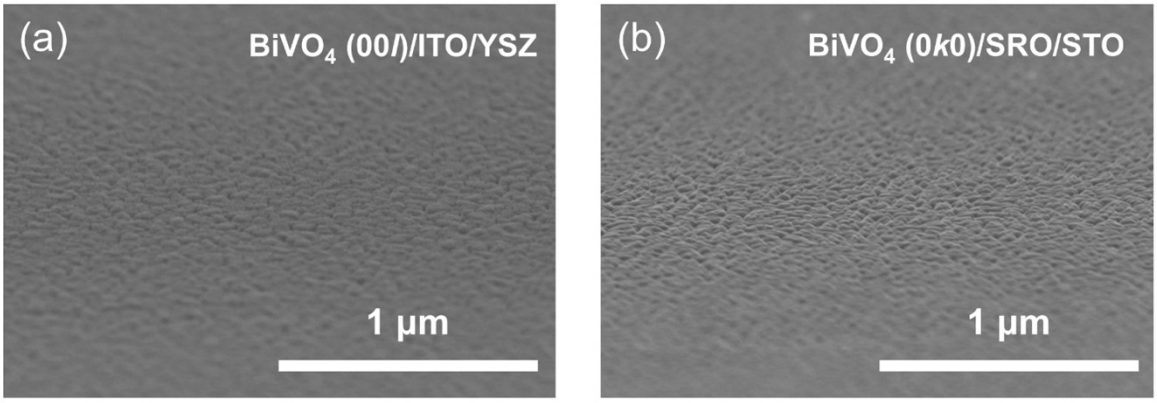

Fig. S6 8˚-Tilted SEM top-surface images of (a) $BiVO_4$ (00*l*) and (b) $BiVO_4$ (0*k*0) thin films, respectively.

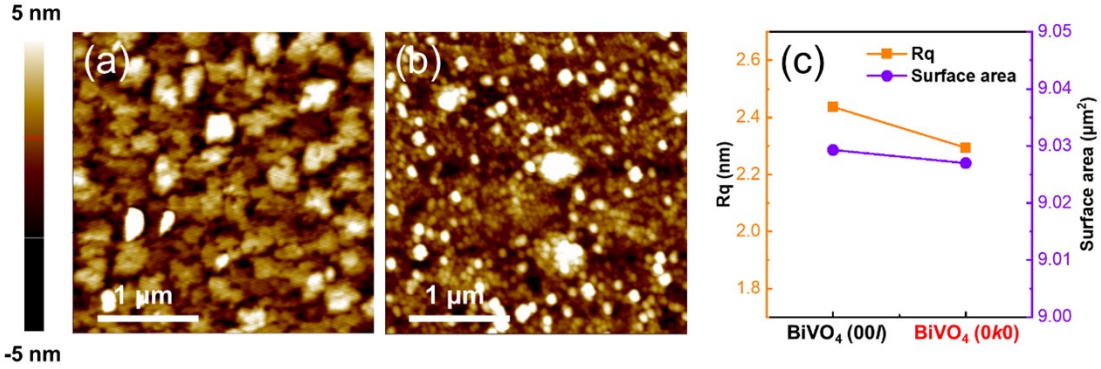

Fig. S7 Topological AFM images of (a) $BiVO_4$ (00*l*) and (b) $BiVO_4$ (0*k*0) thin films. (c) Plot of the root-mean-square-roughness (Rq, left y-axis) and surface areas (right y-axis) of epitaxial $BiVO_4$ thin films with different crystallographic orientations.

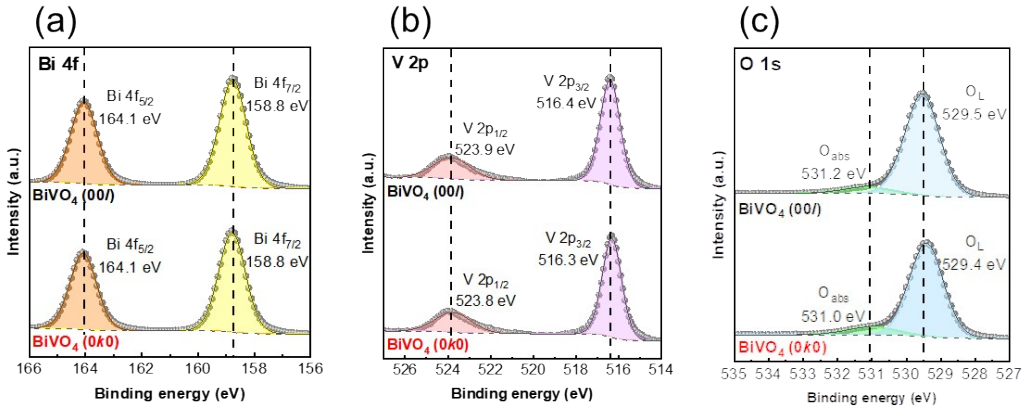

Fig. S8 XPS spectra of (a) Bi 4f, (b) V 2p, and (c) O 1s peaks of $BiVO_4$ (00*l*) and $BiVO_4$ (0*k*0) thin films, respectively.

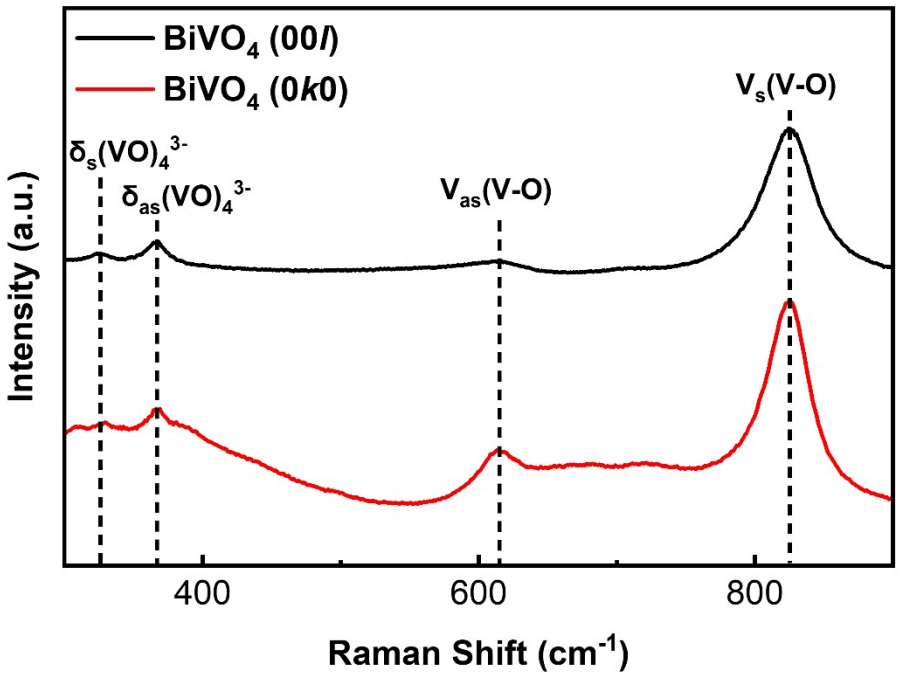

Fig. S9 Raman spectra of epitaxial $BiVO_4$ thin films with (00*l*) and (0*k*0) orientations.

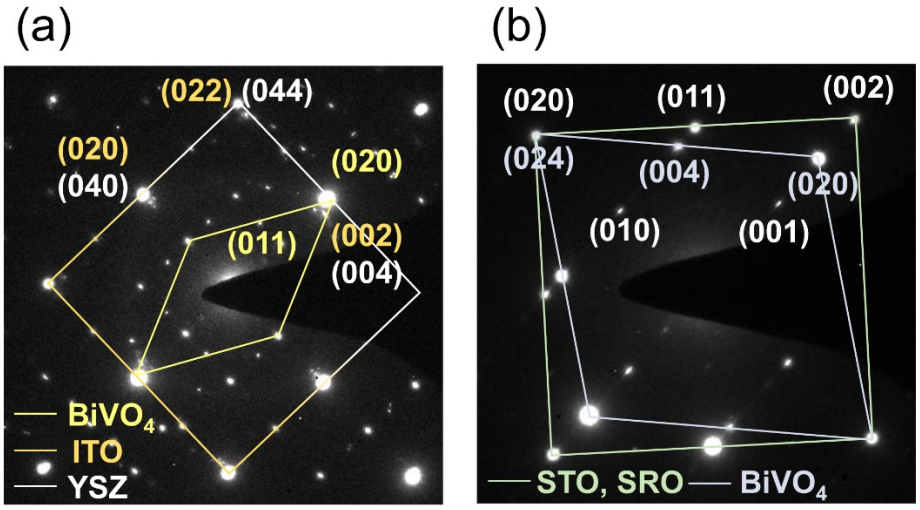

Fig. S10 Magnified selected area electron diffraction (SAED) patterns of (a) epitaxial $BiVO_4$ (00*l*) thin film grown on ITO buffered YSZ (001) substrate and (b) epitaxial $BiVO_4$ (0*k*0) thin film grown on SRO buffered STO (001) substrate.

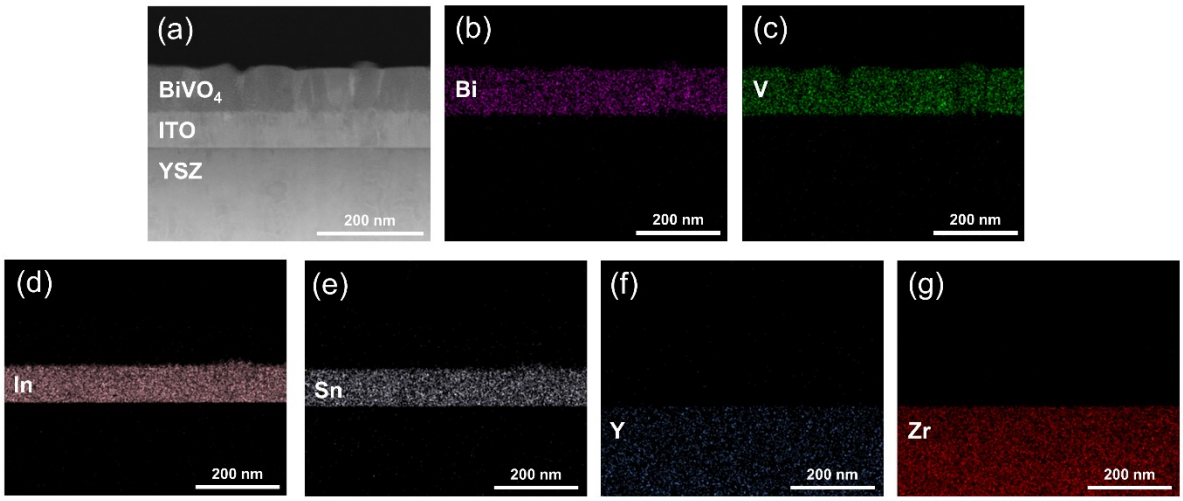

Fig. S11 Cross-sectional TEM image and corresponding EDS elemental mapping of epitaxial $BiVO_4$ (00*l*) thin film. (a) Low-magnification TEM image showing the well-defined layer sequence of $BiVO_4$, ITO, and YSZ. (b–g) Elemental distribution maps of (b) Bi, (c) V, (d) In, (e) Sn, (f) Y, and (g) Zr.

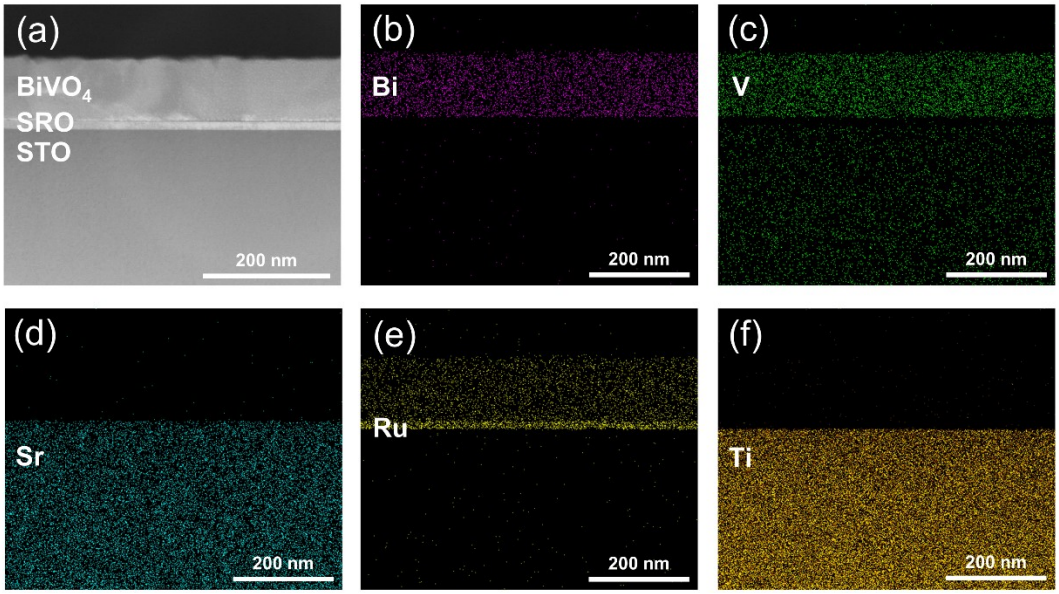

Fig. S12 Cross-sectional TEM image and corresponding EDS elemental mapping of epitaxial $BiVO_4$ (0*k*0) thin film. (a) Low-magnification TEM image showing the well-defined layer sequence of $BiVO_4$, SRO, and STO. (b–g) Elemental distribution maps of (b) Bi, (c) V, (d) Sr, (e) Ru, and (g) Ti.

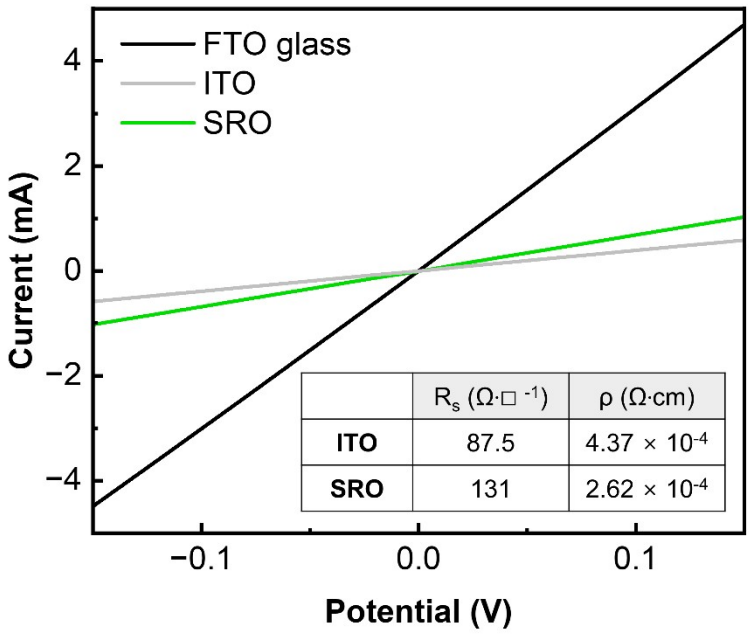

Fig. S13 Current-voltage curves of epitaxial SRO, ITO thin films, and FTO glass substrate measured by the four-point probe.

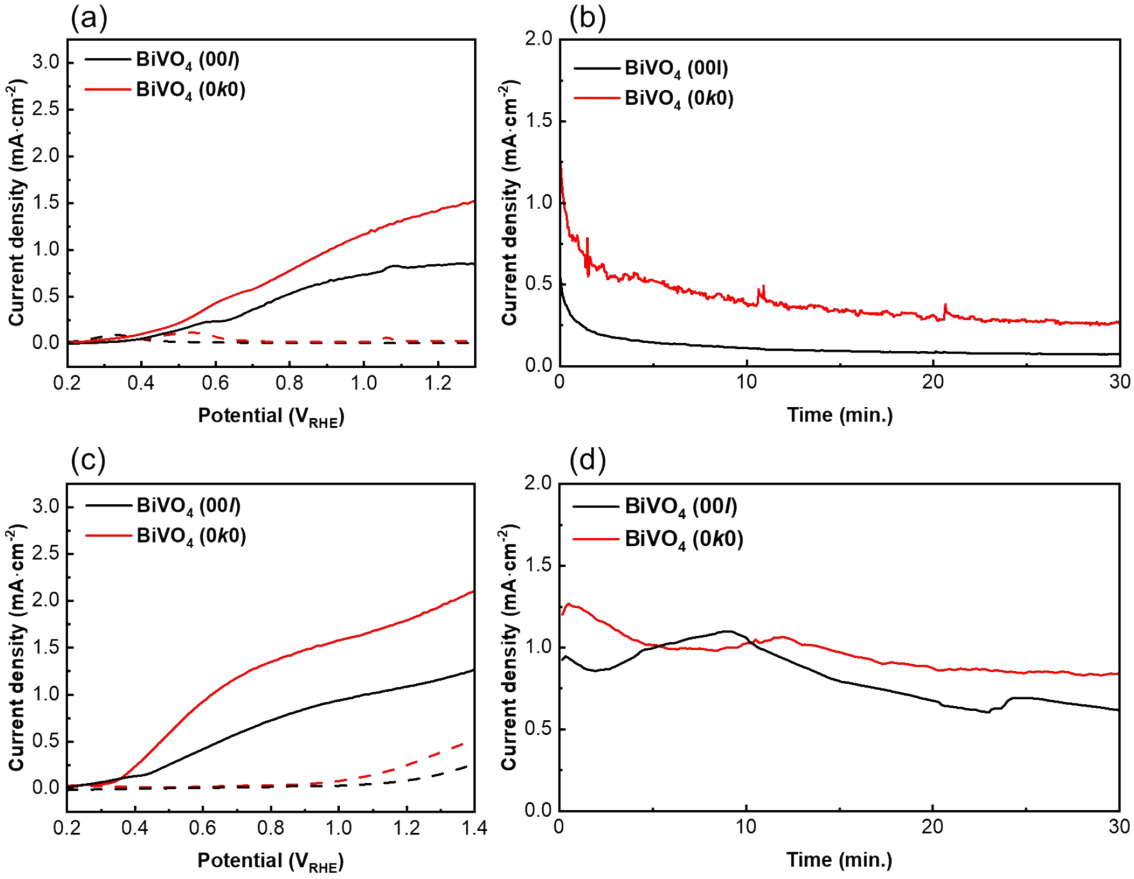

Fig. S14 LSV curves and chronoamperometry analysis (at 1.2 V_{RHE}) of $BiVO_4$ (00*l*) and $BiVO_4$ (0*k*0) photoanodes for PEC glycerol oxidation under AM 1.5G illumination in (a and b) 0.5 M Na_2SO_4 + 1.0 M glycerol (pH ≈ 5.32) and (c and d) 0.1 M HNO_3 + 1.0 M glycerol (pH ≈ 1.03). Dashed lines in (a and c) indicate dark currents. In both electrolytes, the (0*k*0) film consistently delivers higher photocurrent than the (00*l*) film in the LSV profiles and under constant bias operation. The degree of photocurrent decay varies with electrolyte pH and composition, which is consistent with prior reports that $BiVO_4$ can show electrolyte dependent photoanodic instability under anodic bias, frequently accompanied by preferential vanadium leaching, and that suppressing V dissolution using V^{5+} containing electrolytes can mitigate photocorrosion.
3-5

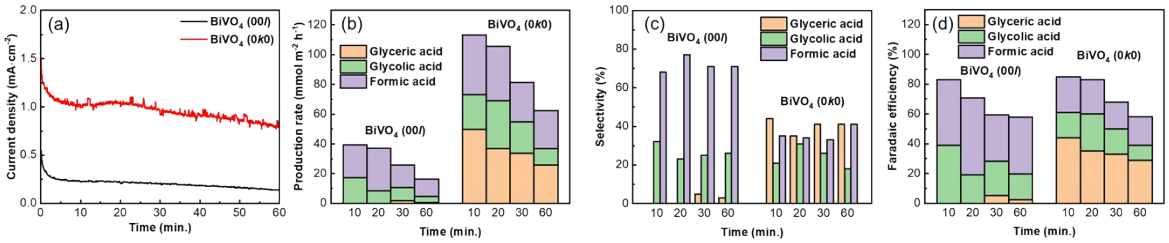

Fig. S15 (a) Chronoamperometry analysis measured at 1.0 V_{RHE} in 0.1 M KOH + 1.0 M glycerol under AM 1.5G illumination, (b) time dependent production rates, (c) selectivity, and (d) faradaic efficiency for glyceric acid, glycolic acid, and formic acid quantified by HPLC during PEC glycerol oxidation at 1.0 V_{RHE}.

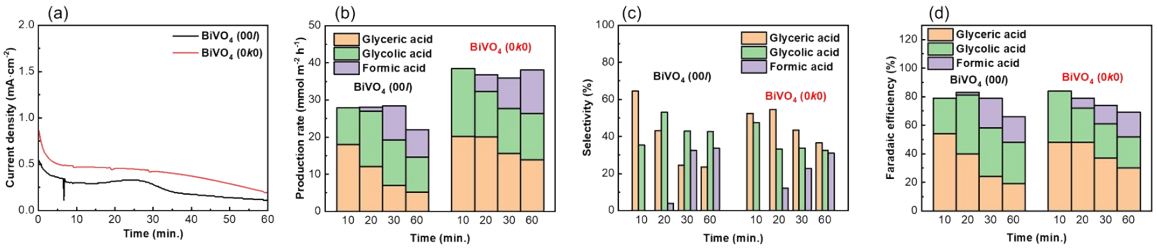

Fig. S16 (a) Chronoamperometry analysis measured at 0.8 V_{RHE} in 0.1 M KOH + 1.0 M glycerol under AM 1.5G illumination, (b) time dependent production rates, (c) selectivity, and (d) faradaic efficiency for glyceric acid, glycolic acid, and formic acid quantified by HPLC during PEC glycerol oxidation at 0.8 V_{RHE}.

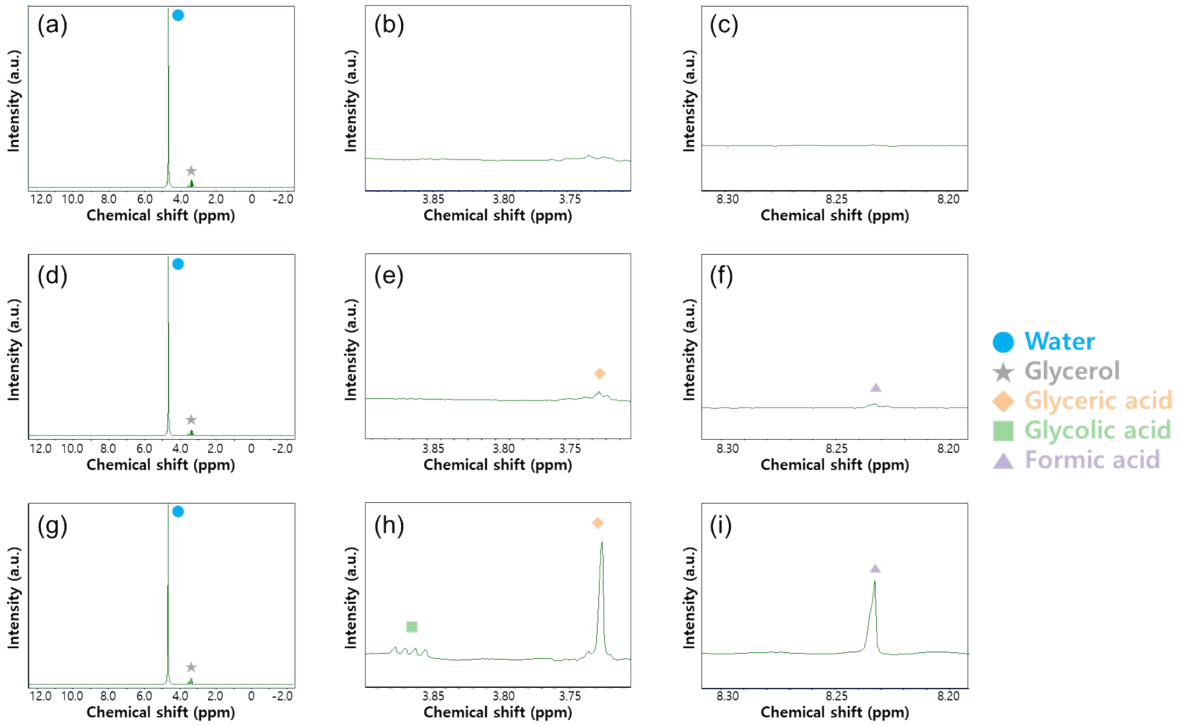

Fig. S17 ^{1}H NMR spectra of the electrolytes collected for qualitative identification of glycerol oxidation products. Bare electrolyte containing 0.1 M KOH + 1.0 M glycerol before PEC operation (a–c), and post reaction electrolytes after PEC operation at 1.0 V_{RHE} for 30 min using $BiVO_4$ (00*l*) (d–f) and $BiVO_4$ (0*k*0) (g–i) photoanodes. Panels (a, d, g) show the full spectra, while (b, e, h) and (c, f, i) display expanded regions highlighting diagnostic resonances assigned to glyceric acid, glycolic acid and formic acid, respectively. It shows characteristic resonances attributable to glyceric acid, glycolic acid, and formic acid, supporting the product identities assigned from HPLC.

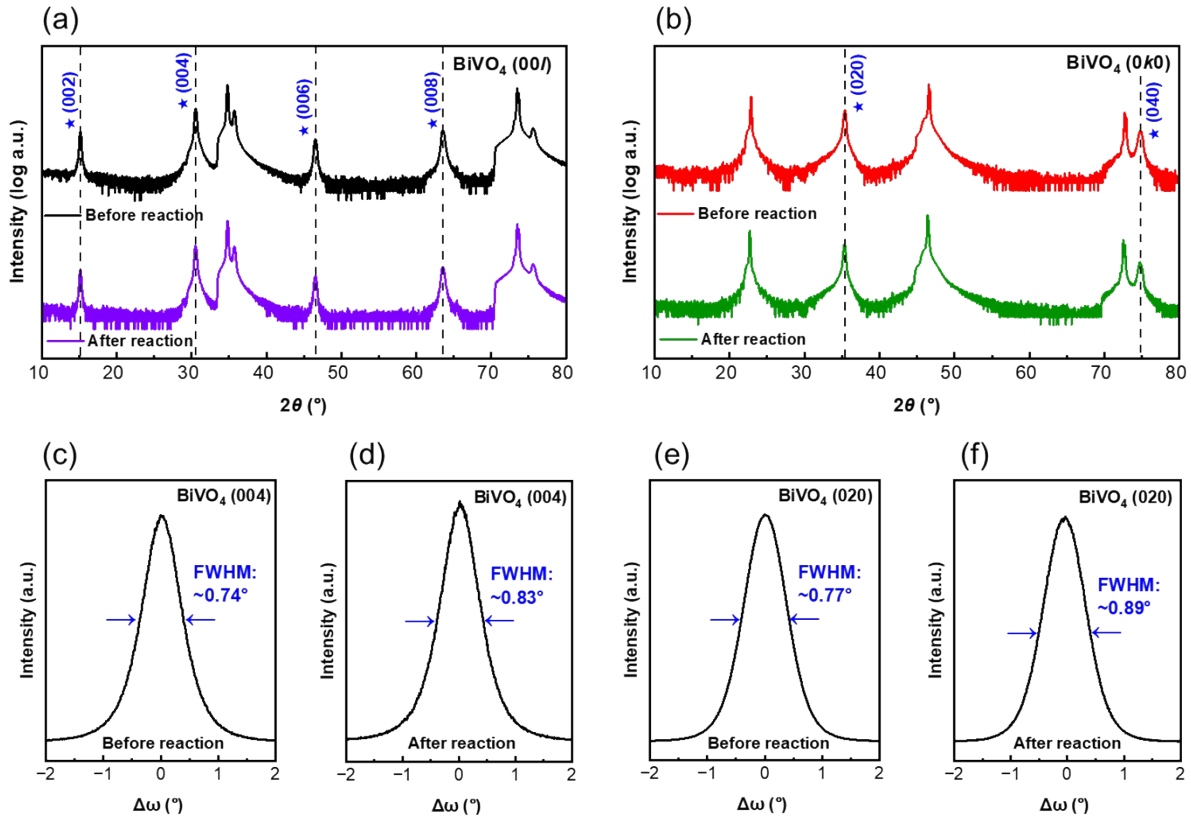

Fig. S18 (a and b) Out-of-plane X-ray diffraction (XRD) θ–2θ scans of epitaxial $BiVO_4$ thin films measured before and after PEC glycerol oxidation, showing (a) the (00*l*)-oriented $BiVO_4$ film and (b) the (0*k*0)-oriented $BiVO_4$ film. (c–f) XRD reflection rocking curves acquired from the (c and d) $BiVO_4$ (004) diffraction peak for the (00*l*) film and (e,f) $BiVO_4$ (020) diffraction peak for the (0k0) film, measured (c and e) before and (d and f) after reaction. The out-of-plane XRD patterns and rocking curve analyses were compared before and after PEC glycerol oxidation to evaluate possible structural degradation. The θ–2θ scans (Fig. S18a and b) show no noticeable shift of the $BiVO_4$ reflections after reaction for both orientations, indicating that the epitaxial phase and out of plane lattice spacing are largely preserved. The rocking curve profiles (Fig. S15c–f) show only modest broadening of the FWHM, from 0.74° to 0.83° for the (00*l*) film and from 0.77° to 0.89° for the (0*k*0) film, suggesting a slight increase in mosaicity while maintaining the overall crystalline integrity of the epitaxial films.

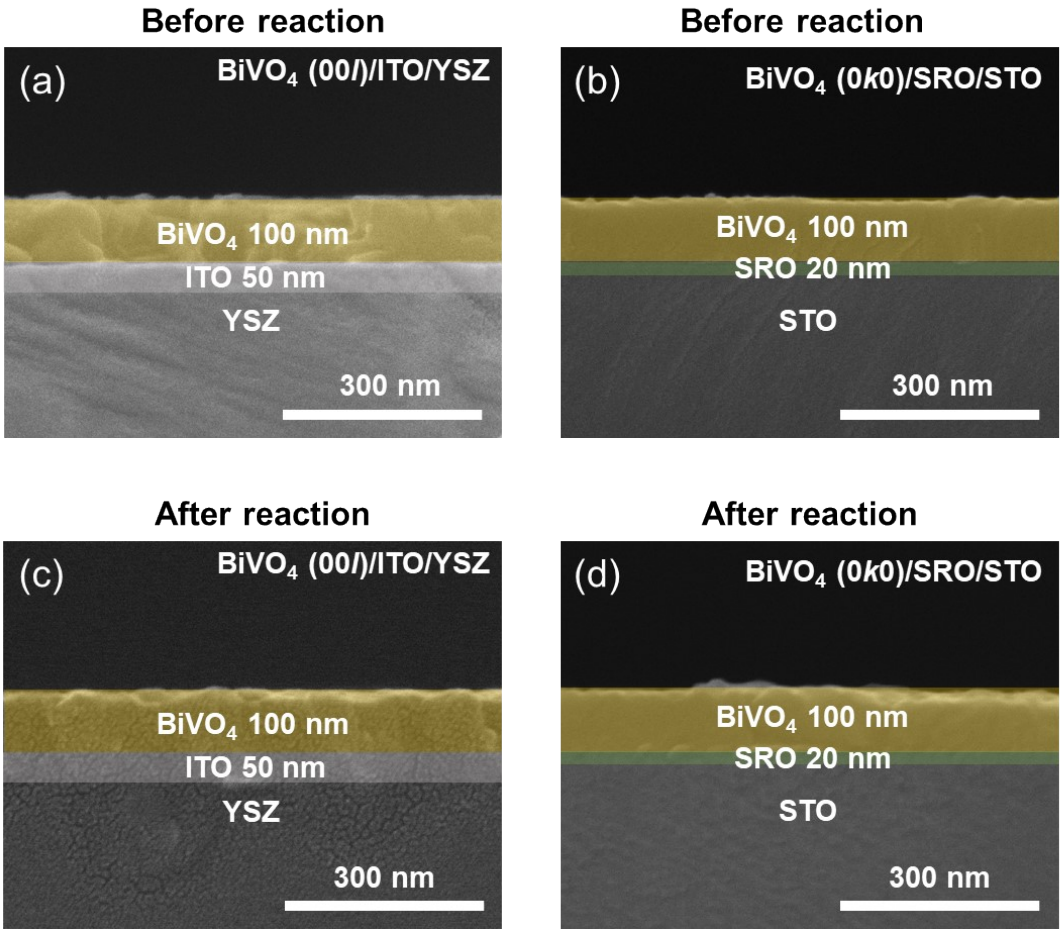

Fig. S19 SEM cross-sectional images of $BiVO_4$ (00*l*) and $BiVO_4$ (0*k*0) thin films (a and b) before and (c and d) after PEC glycerol oxidation. Cross sectional SEM images were compared before and after PEC operation to examine whether photocurrent decay is accompanied by macroscopic structural damage or thickness loss. The images show no obvious change in film thickness or the overall layer architecture for either orientation, indicating that the epitaxial framework remains physically intact after operation.

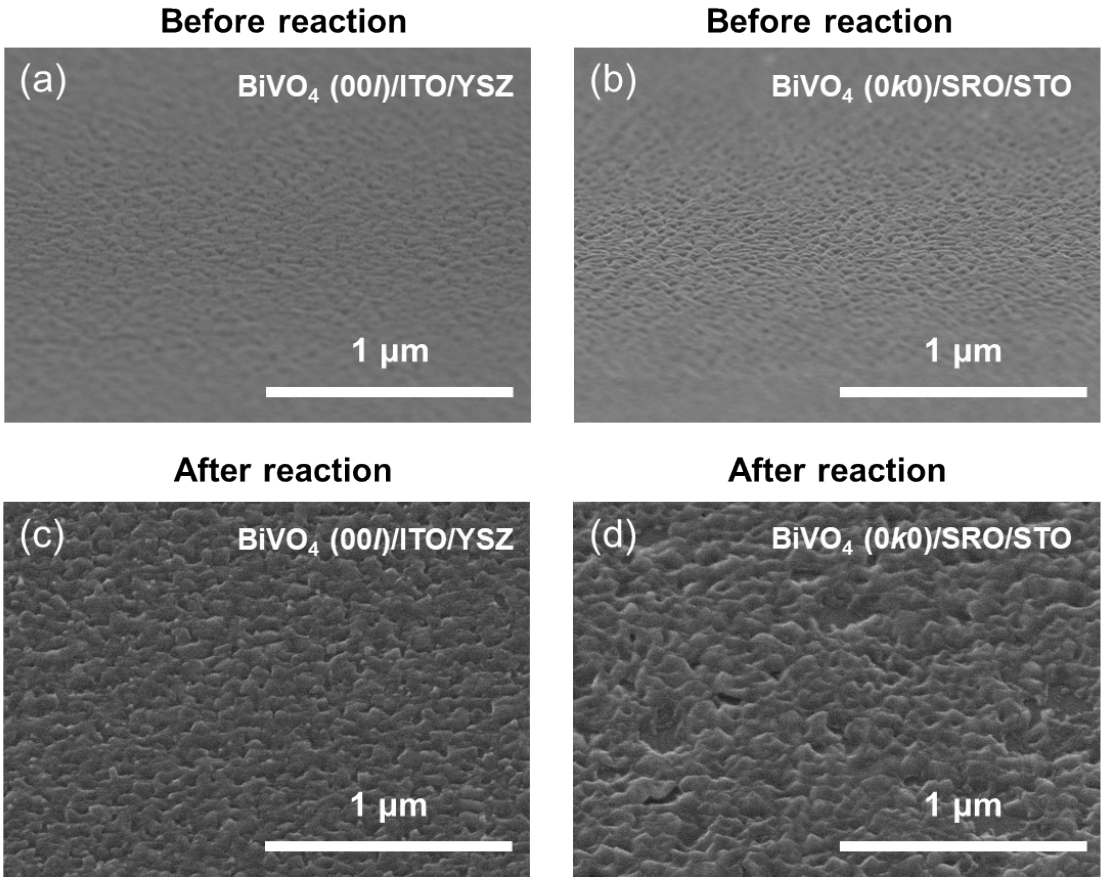

Fig. S20 8˚-Tilted SEM top-surface images of $BiVO_4$ (00*l*) and $BiVO_4$ (0*k*0) thin films (a and b) before and (c and d) after PEC glycerol oxidation. To probe more subtle surface level changes, tilted view SEM top surface images were further collected before and after reaction. After PEC operation, both films exhibit a mild increase in surface corrugation and roughened texture compared with the pristine surfaces, consistent with gradual surface reconstruction or the accumulation of surface species under anodic conditions.

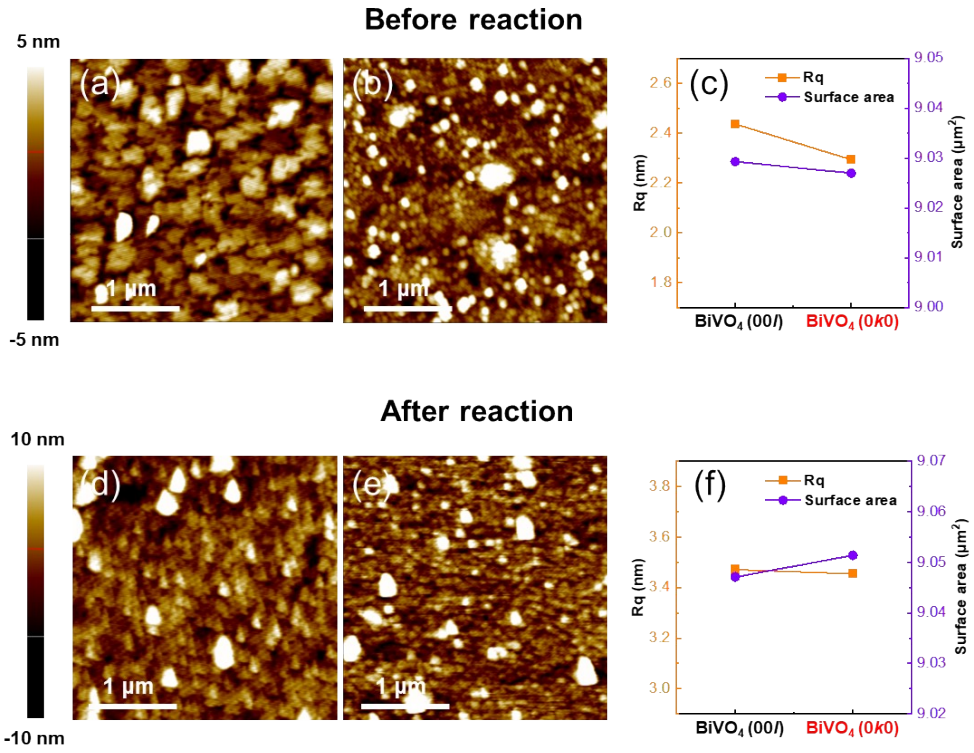

Fig. S21 Topographical AFM images of epitaxial $BiVO_4$ thin films with different crystallographic orientations before and after PEC operation. (a and b) $BiVO_4$ (00*l*) and $BiVO_4$ (0*k*0) before reaction. (c) Root-mean-square roughness (Rq, left axis) and surface active area (right axis) of the films before reaction. (d and e) $BiVO_4$ (00*l*) and $BiVO_4$ (0*k*0) after reaction. (f) Rq (left axis) and surface active area (right axis) of the films after reaction. AFM measurements further corroborate the surface roughening trend after PEC operation. The Rq increases from 2.437 to 3.471 nm for $BiVO_4$ (00*l*) and from 2.294 to 3.455 nm for $BiVO_4$ (0*k*0), while the surface active area changes only slightly from 9.029 to 9.047 μm^2 for (00*l*) and from 9.027 to 9.051 μm^2 for (0*k*0), as summarized in Table S3. These results indicate that PEC operation primarily increases surface corrugation without a significant change in effective surface area within the scanned region.

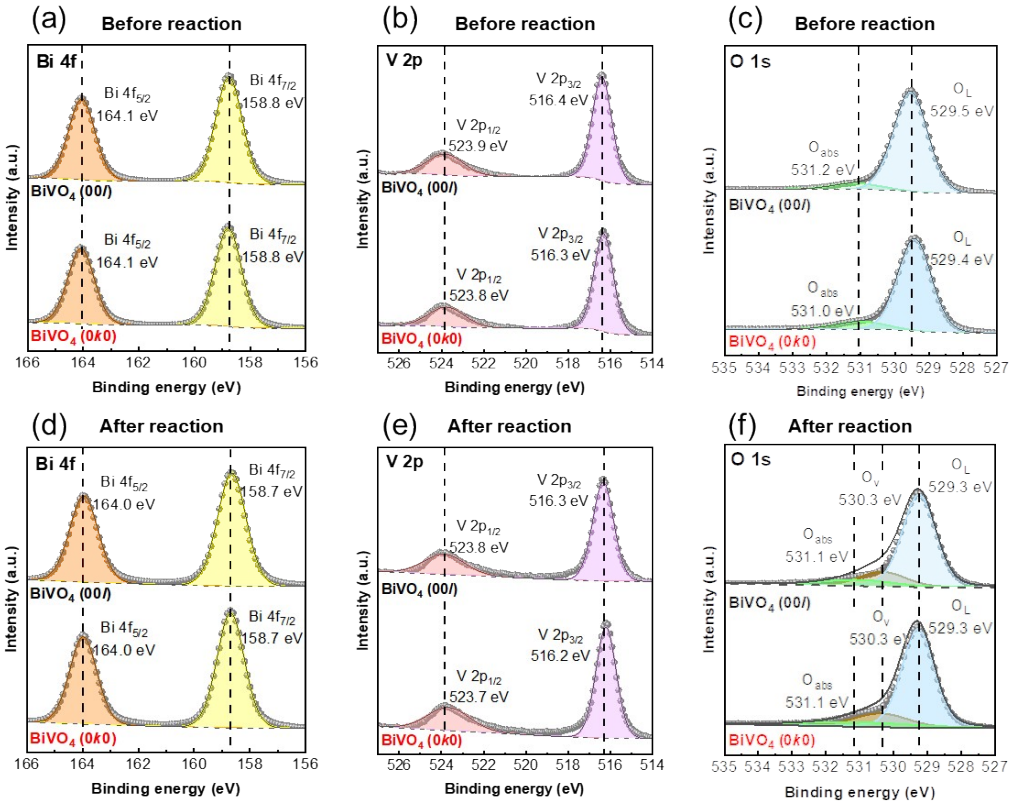

Fig. S22 XPS spectra of epitaxial $BiVO_4$ (00*l*) and $BiVO_4$ (0*k*0) thin films before and after PEC operation. (a,d) Bi 4f, (b,e) V 2p, and (c,f) O 1s core level spectra measured before reaction (a–c) and after reaction (d–f), respectively. XPS spectra collected before and after PEC operation show broadly consistent core level features, indicating that the dominant chemical states are retained, while noticeable compositional evolution occurs at the surface. The survey based elemental composition reveals a decrease in vanadium content after reaction for both films. As summarized in Table S4, the V atomic percentage decreases from 12.58% to 10.99% for $BiVO_4$ (00*l*) and from 12.15% to 11.91% for $BiVO_4$ (0*k*0), consistent with vanadium leaching as a primary compositional change under strongly alkaline anodic operation. In addition, the O 1s spectra show an increased contribution near 530.3 eV together with an enhanced high binding energy component after reaction, which is consistent with the formation of oxygen deficient environments and the accumulation of chemisorbed oxygen containing species on the surface during PEC operation.

Table S1. Production rate, selectivity and faradaic efficiency (FE) of glyceric acid, glycolic acid, and formic acid quantified during PEC glycerol oxidation using $BiVO_4$ (00*l*) and $BiVO_4$ (0*k*0) photoanodes at 1.0 V_{RHE} as a function of reaction time.

Sample	Time (min.)	Product	Production rate [mmol $m^{-2} \cdot h^{-1}$]	Selectivity (%)	FE (%)
$BiVO_4$ (00*l*)	10	glyceric acid	-	-	-
		glycolic acid	17.2	32	39
		formic acid	22.3	68	44
	20	glyceric acid	-	-	-
		glycolic acid	8.4	23	19
		formic acid	28.7	77	51.7
	30	glyceric acid	1.7	5	5.3
		glycolic acid	8.9	25	23
		formic acid	15.2	71	31
	60	glyceric acid	0.5	3	2.3
		glycolic acid	4.2	26	17.3
		formic acid	11.7	71	38.3
$BiVO_4$ (0*k*0)	10	glyceric acid	49.7	44	44
		glycolic acid	23.5	21	17
		formic acid	40.1	35	24
	20	glyceric acid	37	35	35
		glycolic acid	32.2	31	25
		formic acid	36.3	34	23
	30	glyceric acid	33.7	41	33
		glycolic acid	21.1	26	17
		formic acid	26.6	33	18
	60	glyceric acid	25.9	41	29
		glycolic acid	11	18	10
		formic acid	25.6	41	19

Table S2. Production rate, selectivity and faradaic efficiency of glyceric acid, glycolic acid, and formic acid quantified during PEC glycerol oxidation using $BiVO_4$ (00*l*) and $BiVO_4$ (0*k*0) photoanodes at 0.8 V_{RHE} as a function of reaction time.

Sample	Time (min.)	Product	Production rate [mmol $m^{-2} \cdot h^{-1}$]	Selectivity (%)	FE (%)
$BiVO_4$ (00*l*)	10	glyceric acid	18.8	64.5	54
		glycolic acid	9.9	35.5	25
		formic acid	-	-	-
	20	glyceric acid	12.1	43.1	40
		glycolic acid	14.9	53	41
		formic acid	1.1	3.9	2
	30	glyceric acid	7	24.6	24
		glycolic acid	12.2	43	34
		formic acid	9.2	32.4	21
	60	glyceric acid	5.2	23.6	19
		glycolic acid	9.4	42.7	29
		formic acid	7.4	33.6	18
$BiVO_4$ (0*k*0)	10	glyceric acid	20.2	52.5	48
		glycolic acid	18.3	47.5	36
		formic acid	-	-	-
	20	glyceric acid	20.1	54.6	48
		glycolic acid	12.2	33.2	24
		formic acid	4.5	12.2	7
	30	glyceric acid	15.6	43.5	37
		glycolic acid	12.1	33.7	24
		formic acid	8.2	22.8	13
	60	glyceric acid	13.9	36.5	30
		glycolic acid	12.4	32.5	22
		formic acid	11.8	31	17

Table S3. Surface roughness and surface-active area of epitaxial $BiVO_4$ thin films with different crystallographic orientations before and after PEC operation.

	Before reaction		**After reaction**	
Sample	$BiVO_4$ (00*l*)	$BiVO_4$ (0*k*0)	$BiVO_4$ (00*l*)	$BiVO_4$ (0*k*0)
Rq (nm)	2.437	2.294	3.471	3.455
Surface area (μm^2)	9.029	9.027	9.047	9.051

Table S4. The elemental composition of Bi, V, and O in the overall XPS survey spectra of $BiVO_4$ (00*l*) and (0*k*0) films before and after PEC glycerol oxidation.

Sample	Bi (%)	V (%)	O (%)
$BiVO_4$ (00*l*) – before reaction	20.76	12.58	66.66
$BiVO_4$ (00*l*) – after reaction	21.51	10.99	67.49
$BiVO_4$ (0*k*0) – before reaction	20.52	12.15	67.33
$BiVO_4$ (0*k*0) – after reaction	20.43	11.91	67.67

Table S5. Comparison of reported PEC glycerol oxidation performances using bare $BiVO_4$ photoanodes under AM 1.5G illumination, summarizing photoanode structure, crystallinity, electrolyte, charge separation efficiency (η_{sep}) at 1.23 V_{RHE}, donor density (N_D), and photocurrent density measured at 1.23 V_{RHE}.

Structure	Crystallinity	Electrolyte	η_{sep}	N_D (cm^{-3})	Photocurrent density ($mA \cdot cm^{-2}$)	Ref
Porous nanostructure	polycrystalline	0.5 M Na_2SO_4 + 0.1 M glycerol	~ 58	3.72×10^{19}	~ 2.65	6
Worm-like nanostructure	polycrystalline	0.1 M NaBi + 0.1 M glycerol	-	-	1.05	7
Patterned film	polycrystalline	0.5 M Na_2SO_4 + 0.1 M glycerol	~ 62	7.54×10^{20}	1.49	8
Coral-like structure	polycrystalline	0.2 M Na_2SO_4 + 1 M glycerol	-	2.67×10^{18}	3.60	9
Nanostructure	polycrystalline	0.5 M Na_2SO_4 + 0.1 M K_2HPO_4/KH_2PO_4 + 0.5 M glycerol	-	-	~ 1.07	10
Nanoporous array	polycrystalline	0.1 M Na_2SO_4/H_2SO_4 + 0.1 M glycerol	-	-	~ 2.2	11
Nanoparticle	polycrystalline	0.5 M Na_2SO_4/H_2SO_4 + 0.1 M glycerol	-	-	~ 0.1	12
Nanoporous array	polycrystalline	0.5 M Na_2SO_4/H_2SO_4 + 0.5 M glycerol	~ 8	-	~ 0.61	13
Randomly-oriented microstructure	polycrystalline	0.1 M NaBi/0.5M H_2SO_4) + 0.1 M glycerol	-	3.5×10^{16}	~ 1.15	14
(010)-predominated microplate	polycrystalline	0.1 M NaBi/H_2SO_4 + 0.1 M glycerol	-	5.7×10^{17}	~ 1.55	14
(00*l*)-oriented epitaxial thin film	**Single-crystalline**	**0.1 M KOH + 1.0 M glycerol**	**31.6**	**1.65×10^{18}**	**1.06**	**This study**
(0*k*0)-oriented epitaxial thin film	**Single-crystalline**	**0.1 M KOH + 1.0 M glycerol**	**82.3**	**2.81×10^{18}**	**2.51**	**This study**

References

1. Y. Kim, J. H. Kim, E. Lee, S. Lee, Y. Jung, Y. Jang, I. Oh, J. B. Hwang, J. Lee and K. Lee, *Advanced Materials*, 2025, e07698.
2. V. Sampath Kumar and M. K. Niranjan, *Journal of Applied Physics*, 2014, **115**.
3. F. M. Toma, J. K. Cooper, V. Kunzelmann, M. T. McDowell, J. Yu, D. M. Larson, N. J. Borys, C. Abelyan, J. W. Beeman and K. M. Yu, *Nature communications*, 2016, **7**, 12012.
4. H. Wen, Z. Pan, X. Wang, K. Li, Q. Wang, J. Luo, H. Fu, L. Zhang and Z. Wang, *Journal of Hazardous Materials*, 2023, **443**, 130187.
5. D. K. Lee and K.-S. Choi, *Nature Energy*, 2018, **3**, 53-60.
6. Z. Xie, X. Liu, P. Jia, Y. Zou and J. Jiang, *Energy Advances*, 2023, **2**, 1366-1374.
7. Y. Liu, H. Shang, B. Zhang, D. Yan and X. Xiang, *ACS Applied Materials & Interfaces*, 2025.
8. S. H. Roh, Y. Li, J. Y. Kim, W. T. Hong, H. Han, C.-W. Jung, Y. M. Choi, G. M. Noh, Y. S. Jang and K. H. Kim, *Applied Catalysis B: Environment and Energy*, 2025, 125600.
9. P. Yang, Q. Chang, Q. Zhang, J. Yu, X. Ji, Y. Zhang, W. Yang, P. Xiao and Y. Zhang, *Journal of Catalysis*, 2025, **446**, 116061.
10. 1J. Xie, B. Tam, Y. Cai, L. Li, Z. Lin, K. Lambrecht, A. A. Bakulin and A. Kafizas, *Inorganic Chemistry Frontiers*, 2025, **12**, 8785-8799.
11. Y. Han, M. Chang, Z. Zhao, F. Niu, Z. Zhang, Z. Sun, L. Zhang and K. Hu, *ACS Applied Materials & Interfaces*, 2023, **15**, 11678-11690.
12. X. Yang, Y. Luo, J. Xue, Z. Yang, T. Feng, W. Shan, H. Zhang and H. Tang, *Journal of Colloid and Interface Science*, 2025, **688**, 317-327.
13. Z. Wu, H. Guo, K. Ren, Y. Wang, H. Zhang, F. Zhang, L. Liu, G. Li and L. Qi, *Advanced Materials*, 2025, e16504.
14. T.-G. Vo, C.-C. Kao, J.-L. Kuo, C.-c. Chiu and C.-Y. Chiang, *Applied Catalysis B: Environmental*, 2020, **278**, 119303.